PCCP
Physical Chemistry Chemical Physics

Accepted Manuscript

This article can be cited before page numbers have been issued, to do this please use: V. H. Gunawan, M. Schäfer and K. Weitzel, *Phys. Chem. Chem. Phys.*, 2026, DOI: 10.1039/D6CP00772D.

This is an Accepted Manuscript, which has been through the Royal Society of Chemistry peer review process and has been accepted for publication.

Accepted Manuscripts are published online shortly after acceptance, before technical editing, formatting and proof reading. Using this free service, authors can make their results available to the community, in citable form, before we publish the edited article. We will replace this Accepted Manuscript with the edited and formatted Advance Article as soon as it is available.

You can find more information about Accepted Manuscripts in the Information for Authors.

Please note that technical editing may introduce minor changes to the text and/or graphics, which may alter content. The journal's standard Terms & Conditions and the Ethical guidelines still apply. In no event shall the Royal Society of Chemistry be held responsible for any errors or omissions in this Accepted Manuscript or any consequences arising from the use of any information it contains.

ROYAL SOCIETY OF CHEMISTRY

rsc.li/pccp

Charge Attachment Induced Transport times two - sequential double-CAIT in $Li_3B_7O_{12}$

View Article Online
DOI: 10.1039/D6CP00772D

Victor H. Gunawan, Martin Schäfer, Karl-Michael Weitzel*

Philipps-Universität Marburg, Chemistry Department; Hans-Meerwein Str. 4, 35043 Marburg, Germany

Corresponding author: weitzel@chemie.uni-marburg.de

Abstract

Two consecutive charge attachment induced transport (CAIT) experiments have been performed on a $Li_3B_7O_{12}$ glass. In the first CAIT experiment, denoted $Rb^+@Li_3B_7O_{12}$, Rb^+ ions replace native Li^+ ions giving rise to corresponding concentration depth profiles of Rb^+ and Li^+. Subsequently, this ion-exchanged sample has been subjected to a second CAIT experiment where Cs^+ ions serve as external ions. This defines a sequential Double-CAIT experiment, here denoted $Cs^+@Rb^+@Li_3B_7O_{12}$. Concentration depth profiles are measured by means of secondary ion mass spectrometry (SIMS) after the first CAIT and after the second CAIT experiment.

While after the first CAIT an ion-exchange zone has formed in which the Rb^+ ions replace part of the native Li^+ ions, the concentration profile after the second CAIT reveals that Cs^+ was able to push Rb^+ and Li^+ ions deeper into the material. Quantitative simulation of the two concentration depth profiles by means of Nernst-Planck-Poisson theory (NPP) allows derivation of diffusion coefficients for Rb^+ and Li^+ as well as their concentration dependence. While $D(Li^+)$ exhibits a pronounced concentration dependence in the 1st and the 2nd CAIT, $D(Rb^+)$ appears concentration independent in the 1st CAIT but exhibits concentration dependence in the 2nd CAIT. This confirms the basic principle of CAIT, in that the external foreign ion probes the energy landscape of the sample of interest, both for a truly native as well as for an ion-exchanged sample. The results suggest that thermal equilibrium is not reached after the 1st CAIT experiment. A detailed analysis further reveals intricate ion-ion interactions connected to the similarity of bulk diffusion coefficients involved.

1. Introduction

Ion exchange (IE) represents a physico-chemical process, where ions of one chemical kind are replaced by ions of another chemical kind. Early application was primarily in the field of analytical chemistry [1,2]. The focus of the current work concerns manipulation of solid-state materials, where native ions in a solid are replaced by foreign ions. IE can be classified into two important groups.

First, we mention thermal ion exchange. Bringing a (solid) glass containing mobile Na^+ ions into contact with a molten salt containing K^+ ions will lead to IE. Na^+ ions diffuse into the molten salt and K^+ ions diffuse into the glass. This constitutes transport enforced by the gradient of chemical potentials. Transport is time dependent and the amount of IE depends on the time for which transport has been allowed. Clearly, this scenario forms the basis for glass hardening [3,4]. In principle, the same IE process can be induced by bringing a solid K^+ containing glass into contact with a solid Na^+ containing glass. Effectively, the transport will be slower in the second case. IE between two solid phases has been the basis for quantification of diffusion coefficients involving the analysis of concentration depth profiles e.g. by means of the radio tracer diffusion technique [5].

Thermal ion exchange as discussed above is inherently a bidirectional transport process. For reasons of electroneutrality for each tracer ion entering the sample in the forward direction some native ion has to leave the sample in the backward direction. The situation is different for electric field assisted ion exchange (EFIE) [6,7]. In EFIE there are two gradients contributing to the flux of ions, i. the gradient of concentrations and ii. the gradient of the electric potential (the

combination of these two represents the gradient of the electrochemical potential). If the latter dominates, EFIE will result in unidirectional transport in the direction of the field. There is a vast literature on both thermal and electric field driven ion exchange motivated in part by the quest for effective diffusion coefficients and in part by the strive for technically superior materials, e.g., optical waveguides or strengthened glass.

View Article Online
DOI: 10.1039/D6CP00772D

A special variation of unidirectional field assisted ion exchange is the charge attachment induce transport (CAIT) technique developed in the authors group [8,9,10]. The CAIT technique allows to exchange native ions against foreign ions attached to the sample from a charge carrier beam. The conceptual advantage of CAIT is that it is inherently free of any electrical blockage effect. If applied to an ion conducting glass, the result of a foreign-ion CAIT experiment is in general a replacement zone, in which native ions have been replaced by the foreign ion. Denoting the native ion as $M1^+$ and the foreign ion as $M2^+$ leads to the descriptive term $M2^+$@$M1^+$-glass to characterize the experiment. Such experiments have been described in detail in the literature. The goal of this work is to go beyond a single CAIT experiment by performing a consecutive second CAIT experiment of the type $M3^+$@($M2^+$@$M1^+$-glass) by applying $M3^+$ ions to the $M2^+$@$M1^+$-glass sample. This will constitute a sequential Double-CAIT experiment. As far as thermal ion exchange is concerned the concept of double ion exchange experiments has been reported in the literature several decades ago [11] in particular in the context of glass hardening [12,13,14] as well as for optical wave guide production [15,16]. Again, the difference for the sequential Double-CAIT proposed here is, that it is based on unidirectional ion transport.

There are two major goals associated with this work. In previous experiments, termed Single-CAIT from here on, it has been demonstrated that the diffusion coefficient of native mobile ions exhibits a pronounced concentration dependence reflecting the energy landscape, while the diffusion coefficient of the foreign ion appeared constant. This holds true as long as the diffusion of the foreign ion is slow compared to that of the native ion [17]. It has been argued that this simply reflects the properties of an instrument function. At the end of a Single-CAIT experiment, however, the former foreign ion has been incorporated into the glass and has thus become part of the new, modified native material. The first goal of the current Double-CAIT experiment is to show that in the $M3^+$@($M2^+$@$M1^+$-glass) experiment the diffusion coefficient, $D(M3^+)$, again appears constant, while both diffusion coefficients, $D(M1^+)$ and $D(M2^+)$, now exhibit concentration dependence. This reflects the fact that $M2^+$@$M1^+$-glass serves as the native sample to the final 2nd CAIT experiment employing $M3^+$ as foreign ions. The second goal concerns the quantification of energy landscapes. Conceptually a slow foreign ion acts as a probe for the native energy landscape of an ion conducting glass. From a scientific point of view the ability to quantify the populated part of site energy distributions, PSED, in amorphous materials constitutes a unique selling point of the CAIT approach [9,18]. Typically, such PSEDs are assumed to be of Gaussian shape and characterized by a FWHM, which is typically several hundred meV. Here, the goal is to demonstrate that the Double-CAIT experiment is able to address the energy landscape of two mobile charge carriers in a sample even in the case where one of the two has been incorporated in an ion-exchange process. As a more subtle detail, this implies the goal to demonstrate that the population distribution of ions subjected to ion-exchange in this case do not reach thermal equilibrium on the time scale of the experiment.

2. Experiment

The experimental section includes in particular i. the preparation of glass samples, ii. the actual CAIT transport experiment and iii. the quantification of concentration depth profiles by means of the secondary ion mass spectrometry (SIMS).

Sample preparation

A lithium borate glass sample of composition 30% Li2O and 70% B2O3 ($Li_3B_7O_{12}$) has been prepared with the melt-quenching technique. Therefore, the lithium carbonate is dried at 110 °C for 12 h and subsequently mixed with boric acid. The mixture is ground in an agate mortar and poured into a platinum crucible. In order to release water and carbon dioxide, the mixture is then slowly heated to a temperature of 1100 °C. The mixture is kept at this temperature for about 2 h such that a homogenous melt is obtained. Subsequently, the melt is poured into a preheated mold at 450°C, about 50°C below the glass temperature. The rapid cooling leads to the formation of a glass in the mold. The glass is relaxed for 15 h at that temperature and then cooled within 3 h to 80°C to prevent the glass from breaking.

After the glass is cooled down it is removed from the mold and cut into slices using a Mecatome T180, PRESI cutting device. Both sides of each slice are polished employing a LaboPol-5, Struers machine. The polishing procedure is performed stepwise with polishing cloths (PT Plan S, CLOEREN TECHNOLOGY GmbH) and paste (6-KD-C3 and 3-KD-C3, Kemet). After the procedure the slices have thicknesses typically between 1 and 3 mm. In order to improve the contact to the copper back side electrode, the back side of the sample is sputter coated with a 100 nm thick platinum layer. For ideal electric contact, the platinum layer is covered with a silver paste (Heat-Away 641-EV, Kager GmbH).

Charge-attachment induced transport

View Article Online
DOI: 10.1039/D6CP00772D

The central transport experiments performed in this work employ the Charge-Attachment Induced Transport (CAIT) technique for generation of concentration depth profiles within an EFIE approach [19,20,21,22,9,10]. Essential aspects of the technique are briefly described. The sample is attached to a single grounded electrode, referred to as the back side of the sample. The front side is illuminated by an ion beam, with the irradiated area defined by a metal mask. As charge carriers from the ion beam softly attach to the surface, the surface is charged and a well-defined surface concentration and electric potential arises, i.e. also an electrochemical potential. The cloud of ions located in front of the surface constitutes an ideal reversible electrode. The gradient of the electrochemical potential drives charge carrier transport through the sample toward the back side electrode. Charge carriers that reach the back side electrode are neutralized there. This constitutes metal deposition and a corresponding current can be measured.

The source potential of the beam ions determines the maximum potential to which the sample surface can be charged. If the surface potential reaches the source potential, the excess ions from the beam are fully decelerated and eventually deflected. After a short time, a quasi-stationary state emerges, in which the number of charge carriers reaching the front surface equals the number neutralized at the back side electrode. Under these conditions, ions from the ion beam replace those that leave their sites near the sample's front surface. If this situation persists for an extended period, spatially extended concentration depth profiles evolve.

Experimental conditions

In the current work, one $Li_3B_7O_{12}$ sample has been subject to two subsequent CAIT experiments. In the first CAIT experiment, the sample has been illuminated by a rubidium (Rb^+) beam for 94.46 h. Subsequently the sample was removed and analyzed in a ToF-SIMS experiment as described below. After the ToF-SIMS experiment, the sample was again mounted in the CAIT setup and a second CAIT experiment with cesium (Cs^+) ions was performed for another 203.12 h. Both CAIT experiments were conducted at 323 K, and the sample was stored inside a plastic beaker between the two CAIT experiments under argon atmosphere to prevent the formation of foreign layer through reaction with molecules in air, e.g. metal oxide layer, and at 278 K in the refrigerator to prevent significant diffusion process taking place. During this time, the CAIT ion optics were cleaned in an aqueous solution of 5% cleaning concentrate Tickopur R 33, DR H STAMM to prevent Rb^+ ions to be further attached in the second experiment. The ion optics were dried at 383 K overnight.

It is expected that the surface potential during the CAIT experiments reached the value of the source potential already after few seconds. The source potential has been set to 15 V. The sample thickness after polishing is 2.325 mm and the illuminated area in both CAIT experiments was 28.26 mm², corresponding a mask diameter of 6 mm. The recorded current at the back side of the sample suggests that 2.52 mC of Rb^+ and 2.28 mC of Cs^+ have been incorporated into the sample. After the second CAIT experiment, the sample is again transferred to the ToF-SIMS chamber to detect a second profile. Prior to the CAIT experiment the activation energy for transport of the Li^+ ions in the glass has been determined to be 0.65 eV in a two electrode reference experiment ensuring DC conditions.

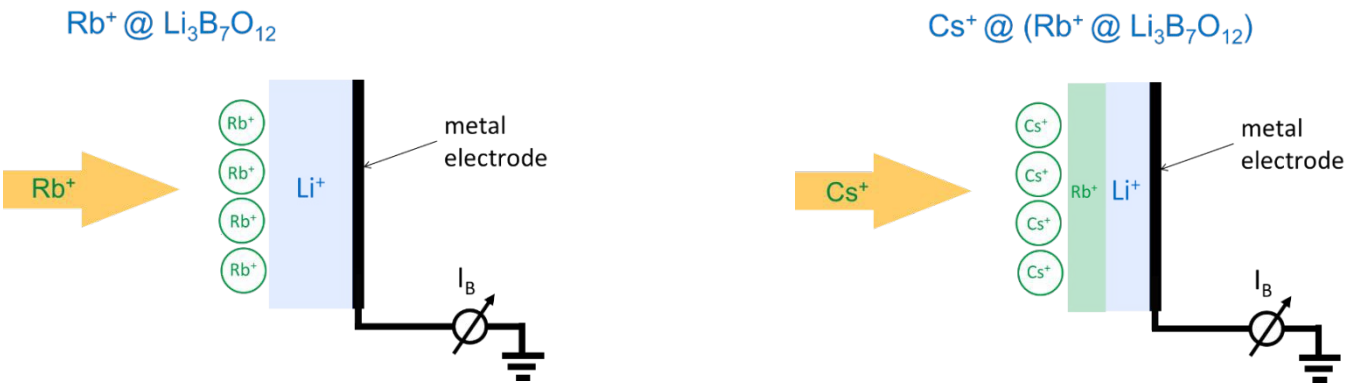

Figure 1: Schematic illustration of Mono-CAIT (left) and sequential Double-CAIT (right).

SIMS-analysis

The concentration profiles are analyzed ex situ employing the time-of-flight secondary ion mass spectrometry (ToF-SIMS) technique, which utilizes two alternative primary ion beams for analysis and sputtering. A Bi^+ beam scans the sample surface within an analysis area of 100 µm × 100 µm, divided into 128 × 128 spots. The Bi^+ ions impinging on the surface with a kinetic energy equivalent to ca. 24000 V induce collision cascades close to the surface of the sample, ultimately leading to the emission of secondary ions and atoms. In this work positively charged secondary ions are extracted and subsequently analyzed in a time-of-flight spectrometer, revealing the local material composition.

Subsequently, an O_2^+ beam is aimed at the surface to ablate the top layer from the sample in an area of 300 µm × 300 µm. Alternating analysis with Bi+ and sputtering with O_2^+ typically 1000 times generates a 3D matrix of mass spectra allowing a reconstruction of the chemical composition in the form of a tomogram. For construction of concentration depth profiles, the mass spectra are summed over the 128 × 128 spots in one layer to obtain the average composition of that layer. Signals of interest for specific m/z ratio are analyzed as a function of the sputter time. The mass resolution is typically m/Dm ≈12000, the depth resolution is typically 2nm. The ablation region is chosen larger than the analysis region to prevent shading effects at the edges of the analysis crater. The measuring device employed was a ToF-SIMS IV/V from Iontof GmbH (Münster, Germany) equipped with an extended dynamic range (EDR) detector. The operating parameters are identical to the ones reported in Gunawan et al.[10].

View Article Online
DOI: 10.1039/D6CP00772D

Normalization procedures

The raw concentration profiles are recorded as Poisson-corrected counts as function of sputter seconds. In order to compare the experimental data to numerical simulations, the sputter seconds have to be transferred to a spatial depth axis while the counts have to be translated into ion concentrations or molar fractions.

The depth axis is calibrated by measuring the crater depth after the ToF-SIMS analysis with a tactile profilometer (Bruker DektakXT). Assuming a constant sputter rate then allows transforming the sputter time into depth. Layer dependent sputter times are routinely checked, but found irrelevant for this work.

Secondary ion yields are in general element specific and depend on the matrix, making also intensity calibration necessary. In order to transfer the Poisson-corrected counts into an absolute concentration, we adopt the normalization procedure described in Gunawan et al. [10]. While this procedure is adequate for the profile obtained after the first CAIT, an extended procedure is required for the second CAIT step, as a third charge carrier species is introduced.

For the second CAIT, the intensity of every ion type is normalized, such that the particle density is conserved throughout the sample, i.e. the sum of all normalized intensities is equal to 1. In the normalization process, the intensities of two most abundant isotopes of an ion type are taken into account, e.g. $^6Li^+$ and $^7Li^+$ for Li, $^{85}Rb^+$ and $^{87}Rb^+$ for Rb. For Cs the $^{133}Cs^+$ is the only stable isotope present in nature. The normalized intensities of Li^+, Rb^+ and Cs^+ are described in the following equations:

$$I_{Li^+,norm} = \frac{I_{6Li^+} + I_{7Li^+}}{I_{6Li^+} + I_{7Li^+} + I_{85Rb^+} + I_{87Rb^+} + I_{133Cs^+}}$$
$$I_{Rb^+,norm} = \frac{I_{85Rb^+} + I_{87Rb^+}}{I_{6Li^+} + I_{7Li^+} + I_{85Rb^+} + I_{87Rb^+} + I_{133Cs^+}} \quad (1)$$
$$I_{Cs^+,norm} = \frac{I_{133Cs^+}}{I_{6Li^+} + I_{7Li^+} + I_{85Rb^+} + I_{87Rb^+} + I_{133Cs^+}}$$

After the normalization, the normalized concentration ranges from 0 to 1 (equivalent to molar fractions), where 1 corresponds to the bulk ion density of $1.4 \cdot 10^{28}$ ions/m³.

3. Theory

Nernst-Planck-Poisson equations

As a basis for the simulations, the coupled set of Nernst-Planck and Poisson (NPP) equations have been used. The theoretical approach has been presented in many publications [20,9,10]. Here, we only review some of the most important aspects to ensure the readability of the manuscript.

The Nernst-Planck equations are solved on a discretized space lattice where the ion flux density J_i for ion species *i* is given by

$$J_i = -D_i(n_i) \cdot \left(\nabla n_i + \frac{Z_i e}{k_B T} n_i \nabla \phi\right). \quad (2)$$

The ion translocation is driven by a concentration gradient ∇n_i and a potential gradient $\nabla \phi$. The diffusion coefficients are generally concentration dependent $D_i(n_i)$. A detailed discussion of the diffusion coefficient is given below. The

charge of the ions is given by the charge number times the elementary charge $Z_i\ e$ while k_BT is Boltzmann's constant times the temperature. Alternatively, the NPP could be implemented in the domain of activities. Here, the NPP equations have been implemented in the domain of particle densities [20,10] and the diffusion coefficients are equivalent to diffusion coefficients derived from DC experiments [21]. Alternatively, the NPP could be implemented in the domain of activities. Possible implications have been discussed by Schäfer et al. [18].

View Article Online
DOI: 10.1039/D6CP00772D

The electric potential is self-consistently defined by the position dependent charge carrier concentration, n_i, and the negative background charge of the background glass matrix, $-n^0$. The absolute value of the background charge equals locally the sum of the charges of the mobile charge carriers and leads to an initially electro-neutral sample. The motion of the cations can then locally lead to small deviation from the electro-neutrality. Poisson's equation is used to calculate the electric potential of the actual space dependent charge carrier concentrations.

$$-\epsilon_0\epsilon_r\Delta\phi = \sum_i (n_i - n^0)Z_i e \quad (3)$$

Here, ϵ_0 is the vacuum permittivity, ϵ_r is the relative permittivity. Here, a value of $\epsilon_r = 7$ has been employed. In principle, ϵ_r can be affected in the ion exchange process. However, this effect is considered to be negligible given the uncertainty of the ϵ_r estimated and also the fact that ϵ_r is dominated by the glass network. Rein et al. have shown that the SED of , e.g. LiAGP, NaAGP and KAGP is basically the same within the error limits of the analysis [23]. The charge carriers from the beam enter the sample from the surface of the sample and are positioned in the first space increment in the simulation. As initially the sample is electro-neutral and homogeneous, the deposition of charge gives rise to concentration and potential gradients as the positive charge of the deposited charge carriers leads to a positive potential in the first space increment. The maximum potential in the first increment is defined by the kinetic energy of the ions from the beam which is defined by the source potential U_R. As soon as the surface potential of the sample reaches the source potential the ion deposition ceases until charge carriers are neutralized at the back side of the sample. The last space increment defines the back side of the sample and is in direct contact with the back side electrode. The potential there is fixed to 0 V, neglecting contact potential. The potential and concentration gradients induce cation transport towards the back side electrode. The time dependence of the charge carrier concentrations is given by Fick's second law that accounts for carrier number conservation within the sample.

$$\frac{\partial n_i}{\partial t} = -\nabla J_i \quad (4)$$

All geometric parameters like the thickness of the sample and the area on which the ion beam impinges are defined by the experiment. The same applies to experimental parameters like the sample temperature. The density of mobile charge carriers, the carrier species themselves and parameters as the relative permittivity are given by the composition of the glass. The sole free parameters that enter the simulations are the concentration dependent diffusion coefficients.

The NPP equation are discretized on a lattice. Thus, the Poisson-Equation reads

$$\phi_a = \frac{\sum_i Z_i e\big(n_i(x_a) - n_{i,0}\big)\Delta x_a \Delta x_{a-1,a}\Delta x_{a,a+1} + \varepsilon_0\varepsilon_r\big(\phi(x_{a+1})\Delta x_{a-1,a} + \phi(x_{a-1})\Delta x_{a,a+1}\big)}{\varepsilon_0\varepsilon_r\big(\Delta x_{a-1,a} + \Delta x_{a,a+1}\big)} \quad (5)$$

At the front side, charge carriers are added as long as $\phi_1 > U_R$.
ϕ_0 is lower than ϕ_1, taking into account that a grounded aperture is positioned 8 mm in front of the sample surface. We assume a linear potential drop between sample surface and aperture. Potential steps at the interface are neglected. At the rear end of the sample $\phi = 0$ due to the contact to a grounded electrode. Again, potential steps at the interface are neglected.

Treatment of the diffusion coefficient

In prior work we have introduced a model where the concentration dependence of the diffusion coefficient systematically follows from the energy distribution of the carrier sites [9,18,23,24]. Essentially, the concentration dependent diffusion coefficient is a result of a concentration dependent effective activation energy $E_{act}(n_i)$ for the long-range transport of charge carriers given by

$$D_i(n_i) = D_{i,0} \cdot \exp\left(\frac{-E_{act}(n_i)}{k_B T}\right). \quad (6)$$

The pre-exponential factors $D_{i,0}$ reflect material properties which also includes effective hopping rates. Here, Do is assumed to be constant.

The energy landscape of the glass is illustrated in Figure 2. Subfigure (a) shows that the initial state of the glass before the CAIT experiments. The sites are filled energetically from bottom to top by native charge carriers (blue shaded area), in the current case Li^+. The uppermost occupied site energy reflects the ionic Fermi energy in a zero Kelvin approximation. Note, that the concept of a Fermi energy can not only be applied to electrons but indeed also to ions [25]. The effective activation energy of the Li^+ is given by the energy difference between the ionic Fermi level and an effective energy threshold E_{DC} for the long-range DC transport.

Mathematically the concentration dependent activation energy is implicitly given by equation (7) and (8)

$$n = \int_{-\infty}^{-E_{act}(n)} S(E)dE \quad (7)$$

$$S(E) = S_0 \frac{2}{\Gamma} \sin^2\left(\frac{(E - E_0)}{\Gamma}\right) \quad (8)$$

Where S is the site density, Γ is the effective width, and So is the total density of sites. E_o has been chosen such that for the bulk density, n_{bulk}, the correct activation energy of the bulk is reproduced.

When the ion motion starts those ions with lower activation energy move first such that the charge carrier distribution of the native charge carriers depicted in Figure 2 is depleted from top to bottom such that the effective activation energy increases. The foreign ions from the beam, in the current case Rb^+, enter the sample from the front side and occupy the abandoned Li^+ sites. The site energy distribution from the point of view of the Rb^+ ions is therefore occupied top down such that the sites with the lowest activation barrier are occupied already at the beginning of the experiment. The effective activation energy therefore seems to remain concentration independent for Rb^+ during the first CAIT experiment.

We end up with an energy landscape where the energetically higher states are now occupied by Rb^+ while the energetically lower lying sites are still occupied by Li^+ ions (Subfigure b). Note, that the replacement populations are placed on a common energy axis for illustration purpose only. The effective activation barriers are in general different for different mobile charge carrier species. In general, the energy axis for the two species may be different as well. Depending on how many of the Li^+ ions have been replaced by the Rb^+ ions, the Fermi level of the Li^+-ions may locally vary across the replacement zone, c.f. Figure 3.

In the second CAIT, the sample that has been treated with Rb^+ before is shined on with a Cs^+ ion beam. Since most of the Li^+-ions already moved away from the vicinity of the front surface and only few Li^+ ions with very high activation energies remain in their sites. The effective activation barrier for the Rb^+ ions is smaller than that of the remaining Li^+ ions. As a consequence, the Cs^+ ions mainly replace Rb^+. The procedure is the same as in the first CAIT but this time Cs^+ replaces Rb^+. Hence, Rb^+ ions with low effective activation energies move first and the Rb^+ distribution is depleted from top to bottom. Cs^+ ions occupy the abandoned sites and occupy the SED from top to bottom. As a consequence, the activation barrier for Rb^+ rises while it seems to remain constant for Cs^+. Meanwhile at the diffusion front, Rb^+ is still pushed deeper into material replacing Li^+ in a process similar to the first CAIT. Additionally the presence of Cs^+ allows Li^+ to be further depleted as shown in Gunawan et al.[10]. The result is a concentration dependent D_{Li} and a concentration independent D_{Rb} in the first CAIT and a concentration dependent D_{Li} and D_{Rb} but a concentration

independent D_{Cs} in the second CAIT. Note, that the discussion of replacement by ion exchange is complex and position dependent in the sample.

View Article Online
DOI: 10.1039/D6CP00772D

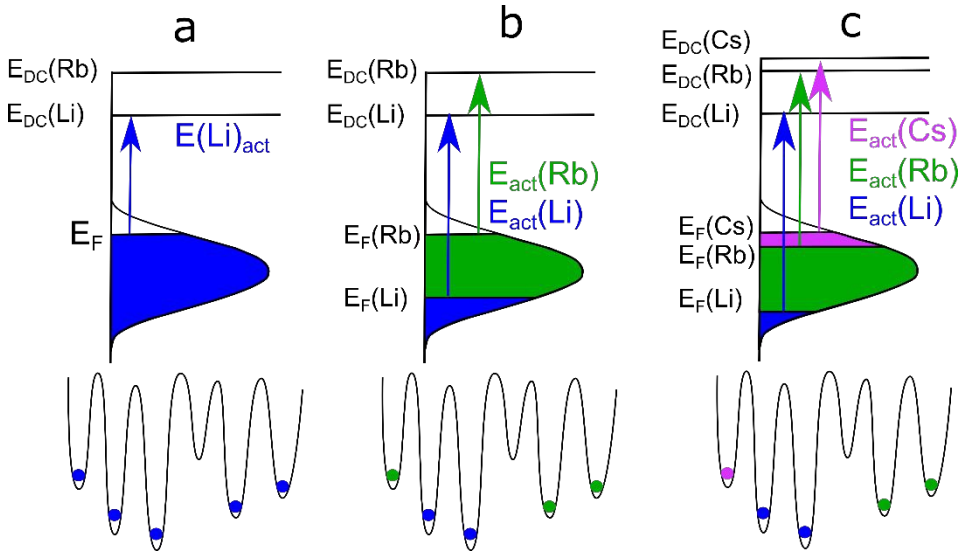

Figure 2: Schematic drawing of the energy landscape before the experiment (a), in the replacement zone after the Rb^+ CAIT (b) and in the replacement zone after the Cs^+ CAIT (c). The effective activation energy of the Rb^+ ions remains constant during the first CAIT and is concentration dependent during the second CAIT.

4. Results and Discussion

First CAIT experiment

During the first part of the experiment the sample has been illuminated by a Rb^+ ion beam for 94.46 h. The Rb^+ ions softly attach to the surface of the sample and lead to a concentration and potential gradient that induces charge carrier transport in the sample - the native Li^+ ions move towards the back side electrode and Rb^+ ions from the beam enter the sample. Essentially, a diffusion zone forms where Li^+ ions have been replaced by Rb^+. Similar experiments have already been presented in the past [22,10]. The diffusion zone remains electro-neutral in very good approximation due to a one-to-one replacement of Li^+ by Rb^+. However, simulations showed a small negative charge excess at the diffusion front. The lack of cations there amounts to about one permille of the bulk ion density. The total density variation at the front is too small to be resolved by the concentration measurements. The presence of a negative charge excess suggests that first Li^+ ions leave their sites and the Rb^+ ions are dragged behind, filling the vacancies.

The results of the first CAIT with a Rb^+ beam agree with the observation in Gunawan et al. [10] within the frame of the error bars. The corresponding concentration profile is shown in Figure 3, Li^+ as blue dots and Rb^+ as green. Evidently, Rb^+ has replaced the Li^+ in a 40 nm zone below the illuminated surface. The smaller size of the diffusion zone compared to Gunawan et al. stems from the lower amount of incorporated charge due to the lower temperature (120 °C compared to 50 °C in the current experiment) and therefore reduced charge carrier mobility. The amount of Li^+ ions remaining in the diffusion zone is close to 10% similar to the work in Gunawan et al. [10]. Thus, this fraction does not vary significantly with the experimental temperature. The black circles show the sum of normalized Li^+ and Rb^+ concentration, which reflects the bulk density in very good approximation throughout the entire sample. This confirms that Rb^+ ions have replaced Li^+ ions in a 1:1 ratio.

Gunawan et al. reported plateaus with basically constant Li^+ and Rb^+ concentration in the diffusion zone [10]. In the current work the concentration profiles exhibit a small slope in the diffusion zone, with highest Rb^+ and lowest Li^+ concentration respectively close to the surface. The reason for that is most likely that the profile has not yet evolved long enough. The plateau characteristic is expected to become more pronounced for a longer diffusion time. Close to

7% of the Li^+ ions remain trapped in their sites and hardly move on the time scale of the experiment. It is estimated that the trapped ions exhibit diffusion coefficients at least two orders of magnitude lower than the rest of the Li population.

View Article Online
DOI: 10.1039/D6CP00772D

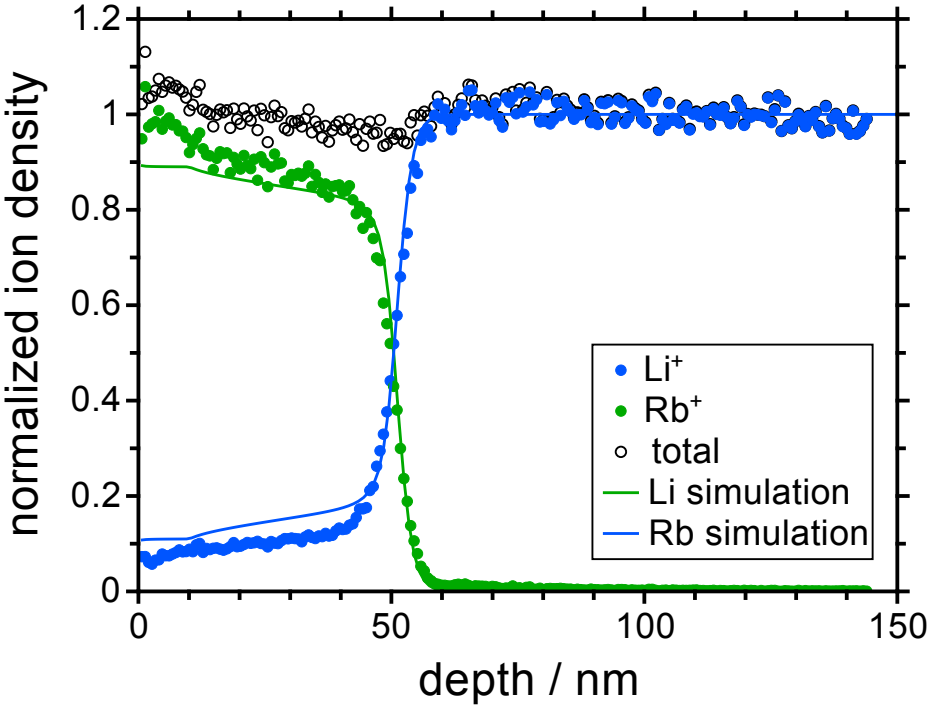

Figure 3: Concentration depth profile after the first CAIT experiment. Rb^+ ions have replaced about 90% of the Li^+ ions within the first 40 nm below the sample surface

The solid lines in Figure 3, show the result of a simulation based on the coupled set of Nernst-Planck and Poisson equations. Beside the geometrical parameters of the sample given in the experimental section, the diffusion coefficients provided in Figure 4 have been used with a pre-exponential factor of $D_{0,Li} = 7.8 \cdot 10^9$ m²/s and a bulk activation energy of $E_{act} = 0.65$ eV for the Li^+ ions and $D_{Rb} = 2.126 \cdot 10^{-22}$ m²/s. The SED used for the lithium ions is the same as published in Gunawan et al., i.e. the mobile part of the Li-SED has a FWHM of 250 meV corresponding to Γ = 0.16 eV [10]. The sample temperature is 50 °C, adjusted to the experimental condition and the source potential is set to 15 V. The simulations confirm that the surface of the sample has been charged to that exact value. Simulation and experiment agree very well. However, the simulation overestimates the amount of Li^+ that remains in the diffusion zone by some few percent. Since the plateau level may vary by few percent when the experiment is repeated with different samples or the profile is evaluated at different sample positions, this deviation is within the error of reproducibility of the experiment. The diffusion coefficient of Lithium in the bulk of the sample is $D_{Li,bulk} = 5.8 \times 10^{-19}$ m²/s. The decrease of D_{Li} below the bulk value applies to the ion-exchange zone, where $n_{Li} < n_{bulk}$.

It is important to note, that the diffusion coefficients of the native glass determined by CAIT are in general agreement with DC conductivities [21].

View Article Online
DOI: 10.1039/D6CP00772D

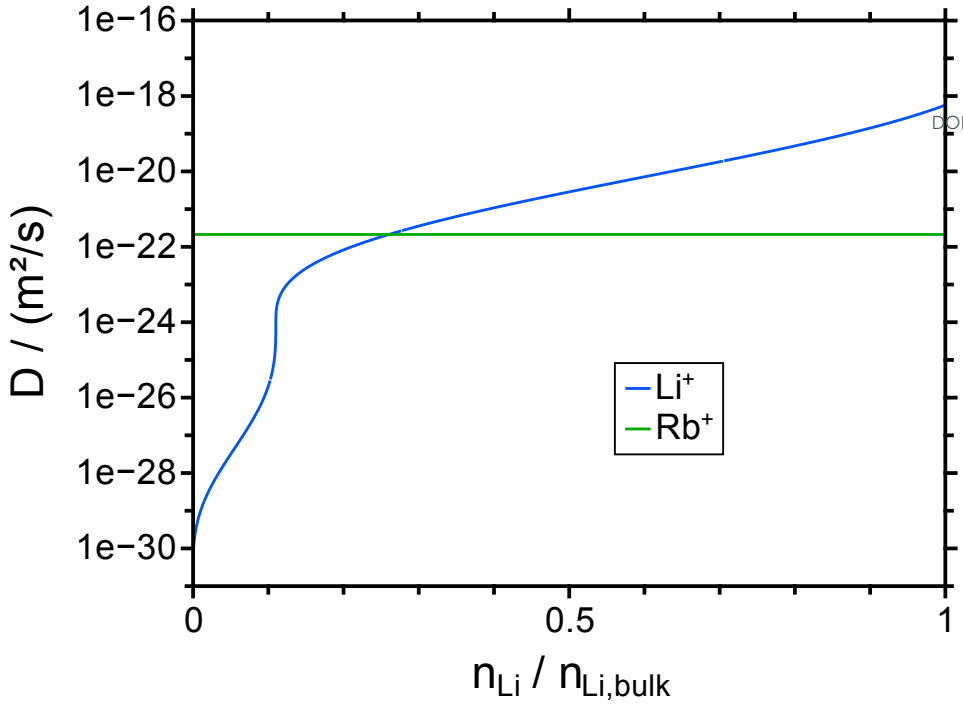

Figure 4: Diffusion coefficient used to simulate the first part of the experiment, i.e. the Rb^+ CAIT on $Li_3B_7O_{12}$. The Lithium diffusion coefficient shows a pronounced concentration dependence.

Second CAIT experiment

After analyzing the concentration profiles of the first (Rb^+)-CAIT via ToF-SIMS, the sample has been placed in the CAIT setup again. Between the two CAIT experiments, the profile of the first CAIT is conserved by cooling the sample. In the CAIT setup the source potential was again set to 15 V and the sample was heated to 323 K. Subsequently, a Cs^+ ion beam was switched on and shined onto the surface of the sample. The geometrical conditions were the same as in the first CAIT. Since the Rb^+ ions replaced most of the Li^+ in zone of approx. 40 nm below the front surface and some Li^+ ions appear trapped in their original sites, the Cs^+ primarily interacts with the Rb^+ ions leading to a zone where Cs^+ has replaced part of the Rb^+ concentration. Analog to the first CAIT, those Rb^+ ions that have low activation barriers move first such that the populated SED of the Rb^+ ions is depopulated from top to bottom. The activation energy for the Rb^+ ions increases with decreasing Rb^+ concentration, hence the diffusion coefficient of Rb^+ decreases with decreasing local concentration. Meanwhile some of the Li^+ ions are trapped and may hardly move. However, the fraction of Li^+ still being effectively trapped in the diffusion zone reduces from 7-10% in the first Mono-CAIT to 3% in the sequential Double-CAIT. Thus, part of the Li^+ ions trapped during the Rb^+ CAIT become effectively mobile during the second part of the Double-CAIT. This is perfectly in line with the observation by Gunawan et al. that also only 3% of the Li^+ ions appeared trapped in the Mono-CAIT employing Cs^+ ions [10]. The findings discussed above imply that the energy landscapes are frozen on the time scale of the experiment and thermodynamic equilibrium is inherently not achieved. Typically, for ion-exchanged systems as discussed in this work equilibration takes place on the time scale of several years [26].

The concentration profiles after the second CAIT are presented in Figure 5.

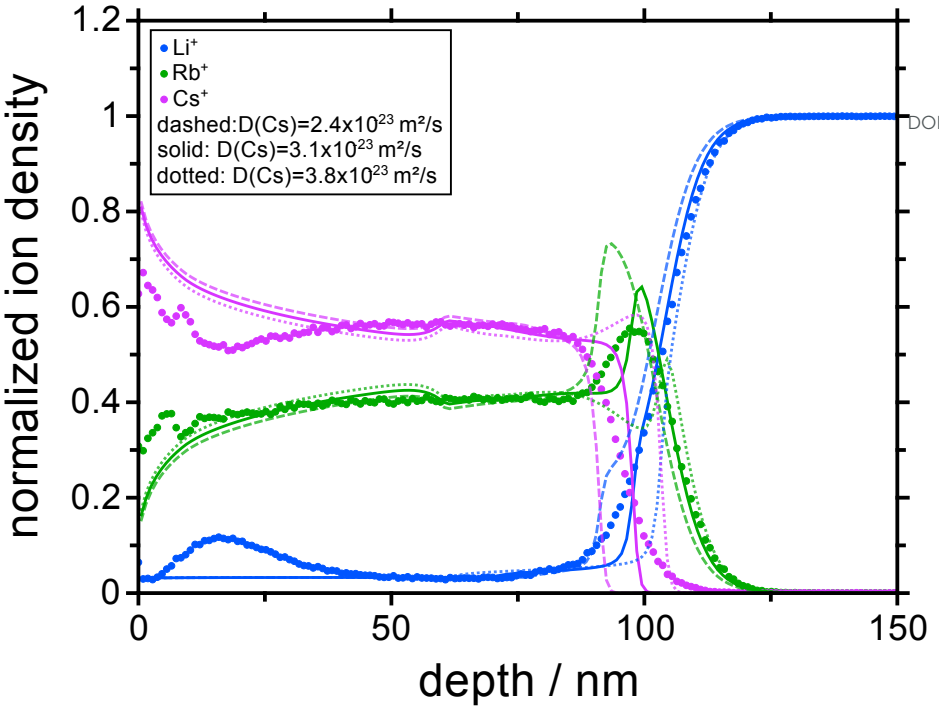

Figure 5: Concentration profile after the second subsequent CAIT experiment. The Cs^+ ions from the second CAIT have replaced a significant part of the Rb^+ ions that entered the sample in the first CAIT experiment. The amount of trapped Li^+ ions decreases from 7-10% to about 3% of the bulk ion density.

The experimentally measured concentration profiles are shown as dots (blue Li, green Rb and purple Cs). Lithium has been replaced as deep as 100 nm below the surface. Both, Rb^+ and Cs^+ are present in the diffusion zone. The sample composition there is on the average 57% Cs^+, 40% Rb^+ and about 3% Li^+. The diffusion zone of Rb^+ reaches 15 nm deeper into the material compared to the diffusion front of the Cs^+. The Rb^+ concentration is higher (57%) between the decay of the Cs^+ trace and the onset of the Li^+ trace and exhibits a local concentration maximum there. An illustration of the temporal evolution of these concentration profiles is provided as supplementary information.

The local maximum in the Li concentration 15 nm below the surface was not observed in repeat measurements. Its origin remains unclear and is considered an artefact at this point. Prior to the first CAIT experiment the polished glass surface is very smooth with a detected surface roughness of about 2 nm (rms). After the first CAIT, the surface roughness has increased to about 5 nm (rms). After the second CAIT the roughness amounts to about 20 nm (rms). Additionally, the sample has been exposed to ambient air when the sample is transferred between the CAIT setup and the ToF-SIMS chamber such that the surface of the sample could be affected. Both, the surface roughness and the exposure to air, may influence the recorded profiles in the vicinity of the front surface. We cannot exclude either of these effects.

The lines in Figure 5 correspond to three calculations with different but concentration independent Cs diffusion coefficients (dashed $D_{Cs} = 2.4 \cdot 10^{-23}$ m²/s, solid $D_{Cs} = 3.1 \cdot 10^{-23}$ m²/s and dotted $D_{Cs} = 3.8 \cdot 10^{-23}$ m²/s) discussed below. Evidently, the main features of the experimental concentration depth profiles are well reproduced by the model calculations. A video of the profile evolution is provided as supplementary material. The Li^+ and Rb^+ diffusion coefficients used in the calculations leading to the profiles shown in Figure 5 are illustrated in Figure *6* and Figure 7. Here, D_{Li} is concentration dependent for both CAIT experiments. At bulk density D_{Li} measures 5.8 x 10^{-19} m²/s. As the Li^+ density drops, D_{Li} decreases about 4 orders of magnitude until a sharp *fall-off* in the diffusion coefficient is observed at 10% bulk density (first CAIT) or 3% bulk density (second CAIT). The concentration dependence of Li used for the calculation was motivated from Gunawan et al.'s work where $Li_3B_7O_{12}$ has been illuminated by K^+, Rb^+ and Cs^+ in Mono-CAIT experiments [10]. A uniform width of the SED for the Li^+ ions was employed. The concentration dependence of D_{Li} for the first CAIT was motivated from the Rb-CAIT and for the second CAIT from the Cs-CAIT in Gunawan et al. [10]. The Li bulk diffusion coefficient has been adjusted to the observed conductivity of the sample at 50 °C (cf. Figure 6). Ultimately, also the concentration dependence of D_{Rb+} exhibits a sharp fall-off, observed at about 10% of the bulk concentration of Li^+.

View Article Online
DOI: 10.1039/D6CP00772D

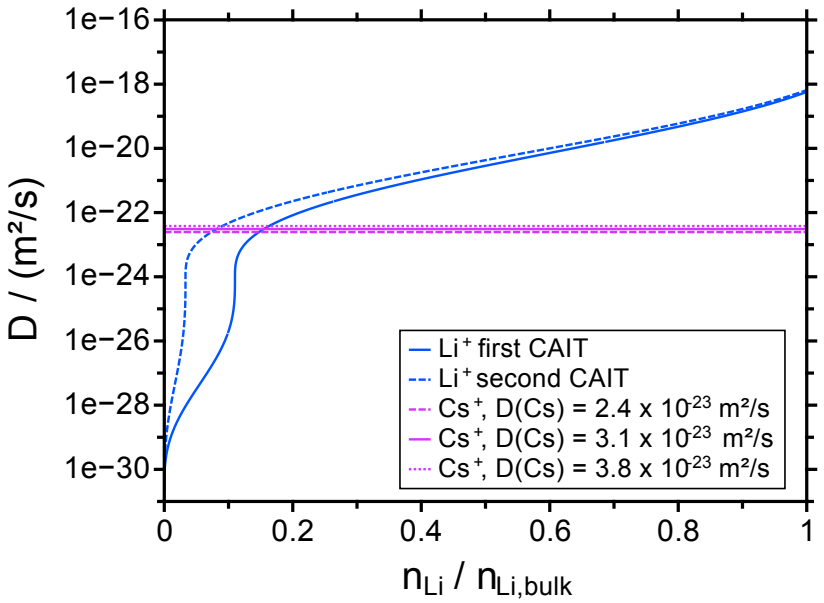

Figure 6: Concentration dependent diffusion coefficient of Li^+ during the first CAIT and the second CAIT (blue sold and blue dashed). The constant diffusion coefficients of Cs^+ for the three calculations shown in Figure 5 in purple.

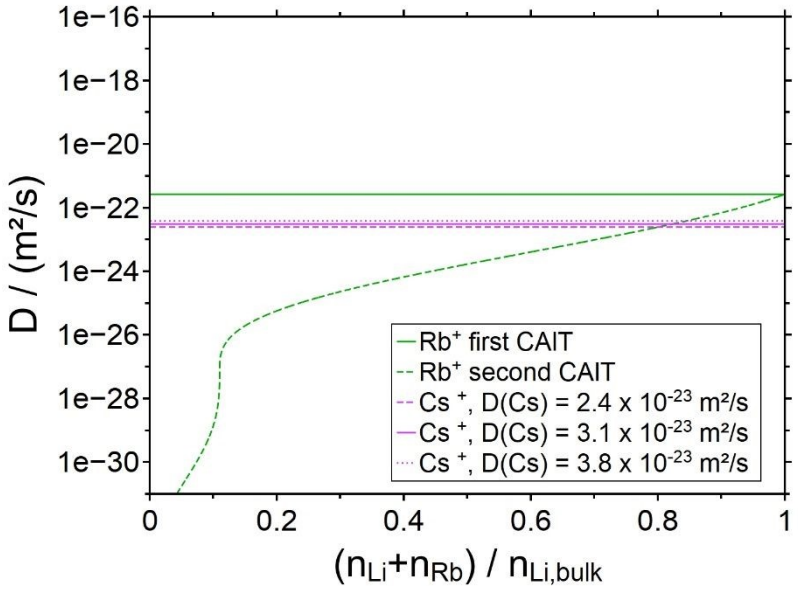

Figure 7: Constant diffusion coefficient of Rb^+ during the first CAIT and concentration dependent Rb^+ diffusion coefficient the second CAIT (blue sold and blue dashed). The constant diffusion coefficients of Cs^+ for the three calculations shown in Figure 5 in purple.

In total, several hundred simulations have been performed with different diffusion coefficients for Rb^+ and Cs^+. The investigated diffusion coefficients include variations of the constant D_{Rb} in the first CAIT, the concentration dependence of D_{Rb} in the second CAIT as well as the concentration independent D_{Cs} in the second CAIT. In neither calculation a local maximum of Li can be observed 10 nm below the sample surface. As the consequence, this weak feature has to be considered an artefact at this point. Such a hump in the Li concentration has not been observed in any other of the experiments conducted in the course of this study. The calculation with $D_{Cs} = 3.1 \cdot 10^{-23}$ m²/s and the D_{Rb} concentration dependence shown in Figure 7 reflects the best match between theory and experiment (see

Table *1* for the full set of parameters). The simulation matches the concentration levels in the diffusion zone qualitatively in a good approximation, in particular the position and slopes of the diffusion fronts of Li and Rb are the same in experiment and theory. The slope of the calculated Cs profile is steeper than the experimental profile but the

position again agrees. The local Rb maximum at the diffusion front amounts to roughly the same accumulation of Rb concentration in experiment and theory (peak area). However, the Rb peak is narrower but higher in the calculation.

View Article Online
DOI: 10.1039/D6CP00772D

Parameters for the best match between experiment and theory (second CAIT)					
First CAIT					
Li		Rb		Cs	
D_{bulk}	5.8 x 10^{-19} m²/s	Constant D	2.67 x 10^{-22} m²/s	n.a.	n.a.
Width SED (FWHM)	250 meV				
Fall of in D	10% $n_{bulk,Li+}$				
Second CAIT					
Li		Rb		Cs	
D_{bulk}	5.8 x 10^{-19} m²/s	D_{bulk}	2.67 x 10^{-22} m²/s	Constant D	3.1·10^{-23} m²/s
Width SED (FWHM)	250 meV	Width SED	225 meV		
Fall off in D	3% $n_{bulk,Li+}$	Fall off in D	10% $n_{bulk,Li+}$		

Table 1: Simulation parameters employed for the best match between experiment and simulation

The simulations indicate that the shapes of the concentration profiles are most sensitive to the exact diffusion coefficients where the magnitudes of D_{Li}, D_{Rb}, and D_{Cs} are comparable. This situation is realized where the Li^+ concentration is already low (about 10-15% of the bulk concentration) and the concentrations of Rb and Cs are similar. In the Figure 5, we find this situation at the diffusion front of Cs. As a consequence, the position and the height of the local maximum of Rb next to the Cs diffusion front strongly depends on all three diffusion coefficients. A variation of D_{Cs} by 20% shows drastic impact on this feature as the three calculations shown in Figure 5 indicate. The profiles are less sensitive to variations of the diffusion coefficient in regions where the respective diffusion coefficients are very different.

The model of a site energy distribution that is depopulated strictly top down for the native ion has been successfully applied describing the ion transport when two charge carriers, one from the beam and one native to the glass, are present [9,24,23]. Even if two different ion species are native to the glass, the NPP calculations yield profiles well in agreement with experiment if the ion beam species and one of the native ion species are identical [18]. In the current work a third ion species comes into play that depletes the population of an ion species that has been introduced by a prior CAIT experiment. The model is excellent at describing the first CAIT. However, when comparing experimental and theoretical profiles of the second CAIT, subtle differences emerge, even though there's good overall agreement in the profile characteristics.

The differences are most significant in particular where the diffusion coefficients of two or even all three species become similar as the competition for the free sites and hence the interaction between different charge carrier species becomes significant. In the profile, this situation is realized in the region between the diffusion front of Cs^+ and the diffusion front of Rb^+, where large concentration variations occur.

At this point it is important to stress the assumptions implied by using classical NPP theory. NPP theory, as currently implemented in the MAR_CCT program suite assumes that ion-ion coupling is restricted to the Poisson level. The findings discussed above are indicative of ion-ion coupling beyond this Poisson level. In classical transport theory, the interaction between different ion species beyond the Poisson level is accounted for by Onsager cross-correlations [27,28,29,30,31] . These coefficients describe the movement of one ion type under the influence of another. These correlations should be large when ions of both types are equally mobile. Therefore, the diffusion coefficients discussed here should be considered effective diffusion coefficients, encompassing contributions from both direct Onsager coefficients and Onsager cross-correlations.

The idea of a Li^+ diffusion coefficient depending solely on the locally remaining Li^+ concentration and a Rb^+ diffusion coefficient depending only on the amount of Cs^+ that has depleted the Rb^+ concentration is most likely too simple. The ionic radii of Li^+, Rb^+, and Cs^+ typically vary with coordination number, measuring approximately 110 pm, 168 pm, and 182 pm respectively [32]. The ions introduced from the beam are therefore much larger than the native Li^+ ions. As the CAIT experiments are operated at temperatures far below the glass transition temperature of $Li_3B_7O_{12}$, the borate

View Article Online
DOI: 10.1039/D6CP00772D

network is relatively rigid. The network operative in the transport experiments is the one adjusted to the number and the size of the Li^+ ions that were present when the glass was formed. Under the condition of the CAIT experiments, the network cannot effectively adjust to the size of the Rb^+ and Cs^+ ions introduced leading to strain near the samples surface. The strain modifies the surface hardness and can for example be detected by nanoindentation measurements [33,34,35]. Technical, the strain introduced by ion exchange is interesting because it leads to surface hardening when a small native ion is replaced by a large foreign ion [3,36]. When the Cs^+ ions arrive at the surface, they experience a surface that has been hardened by Rb^+ compared to the native $Li_3B_7O_{12}$ glass. On the other hand, the hardness does not change significantly across the replacement zone and the Cs^+ ions basically see a constant hardness. Again, directly at the diffusion front, the situation is clearly more complex. At this point, it is argued, that the agreement between experimental and simulated concentration depth profiles is actually surprisingly good. In other words, the effect of ion-ion coupling beyond Poisson must be relatively small. It appears possible that the current sequential Double CAIT experiment is perhaps capable of adding to the understanding of cross-terms in the Onsager matrix of transport coefficients in the future. The current data set does not warrant the derivation of cross Onsager terms. Ultimately, the best access to the full Onsager matrix is expected to be provided in a simultaneous Double-CAIT experiment [37].

In a homogeneous ion conductor containing three mobile ion species, e.g., Li^+, Rb^+ and Cs^+, one might expect all three diffusion coefficients to depend on their respective concentration. In a unidirectional ion exchange experiment with replacement in the forward direction, e.g. the CAIT experiment, it is only the native ions for which a concentration dependence of the diffusion coefficient, D, is observed. In the Mono-CAIT, $D(Li^+)$ was observed concentration dependent. The foreign ion, Rb^+, was dragged behind the Li^+ ions and consequently $D(Rb^+)$ appeared constant. In the sequential Double-CAIT experiment Li^+ and Rb^+ represent native ions which pull the foreign ion Cs^+ behind. As a consequence, now $D(Li^+)$ and $D(Rb^+)$ appear concentration dependent and $D(Cs^+)$ appears constant.

The simulation of the concentration depth profiles shown in Figure 5 is based on Li and Rb populations of the form displayed in Figure 2b, with Rb occupying energetically high-lying states and the remaining Li occupying very low-lying states. Such a distribution is clearly far from thermal equilibrium, where Li and Rb populations would partially mix. In line with their different E_{DC} threshold energies, one would expect Li to occupy, on average, energetically deeper states than Rb. However, the strict energetic separation between Li- and Rb-occupied states should disappear and become smeared out, such that a significant fraction of Rb also occupies sites that lie energetically below the highest Li-occupied state. The good agreement between simulation and experiment indicates that such an equilibrium situation was not realized in the experiment, as it would have led to a different concentration dependence of the Li and Rb diffusion coefficients in the second CAIT experiment. As discussed above, the profiles showed the strongest dependence on the diffusion coefficients when two or even three ion species exhibit diffusion coefficients of roughly the same magnitude. This is precisely the situation in which the strongest interactions between the ions are expected and where a mixing of the populations should occur. We can therefore conclude that equilibration of the populations under the given conditions may only take place on a timescale longer than several months, potentially even years.

5. Summary

A sequential Double-CAIT experiment has been described to provide additional understanding of potential energy landscapes of mobile ions governing long range ion transport in solids. To this end a first CAIT experiment of type $Rb^+@Li_3B_7O_{12}$ introduces an ion exchange zone in a $Li_3B_7O_{12}$ glass. The energy landscape of native Li+ ions derived is in agreement with previous studies [10]. A subsequent second CAIT experiment of the type $Cs^+@(Rb^+@Li_3B_7O_{12})$, probes the energy landscape manipulated in the first CAIT experiment. Theoretical analysis allows to address the energy landscapes of the Li^+ as well as the Rb^+ ions. The FWHM of the two PSEDs is identical within the error limits of the analysis.

As a result of the experiments and theoretical analysis it is possible to conclude that i.) energy landscapes operative for different ion species in the glass do not reach thermal equilibrium, ii.) the energy landscape of ion conductors can not only be determined for native single ion conductors but also for conductors containing replacement zones, iii) the diffusion coefficient of Li^+ can be described by the same Li site-energy distribution in both the first and the second CAIT experiment.

The diffusion coefficients of ions present in a sample upon CAIT impact exhibit concentration dependence, while the diffusion coefficient of the foreign ion always appears constant as long as it is the “slowest” ion in the system.

View Article Online
DOI: 10.1039/D6CP00772D

6. Acknowledgement

Financial support of this work by the DFG through project P1 of the DFG Research Unit Energy Landscapes and Structure of Ion Conducting Solids (We 1330/23 and 24) is gratefully acknowledged. The authors are grateful for stimulating discussions within the ELSICS consortium.

7. Supporting Information

Supporting Information is available in the form of a video file showing the calculated time evolution of all relevant normalized particle densities including the first and the second CAIT experiment (ESI Gunawan et al. density_evolution.mp4). In addition, selected snapshots are provided.

8. Data Availability Statement

The data presented in this work will be made available through a repository (https://doi.org/10.17192/openumr/524).

References

1. R. Kunin and F. McGarvery, *Ind. Eng. Chem.*, 1954, **46**(1), 118.
2. R. Kunin and F.X. McGarvey, *Anal. Chem.*, 1962, **34**(5), 48R-50r.
3. M.E. Nordberg, E.L. Mochel, H.M. Garfinkel and J.S. Olcott, *Journal of the American Ceramic Society*, 1964, **47**(5), 215.
4. A.K. Varshneya, *Int J of Appl Glass Sci*, 2010, **1**(2), 131.
5. Mehrer H, editor, *Diffusion in Solids*: *Fundamentals, Methods, Materials, Diffusion-Controlled Processes,* Springer, Berlin, Heidelberg, SpringerLink Bücher, 155, 2007.
6. J. Fleig, *Phys Chem Chem Phys*, 2009, **11**(17), 3144.
7. A. Talimian, G. Mariotto and V.M. Sglavo, *Int J of Appl Glass Sci*, 2017, **8**(3), 291.
8. J. Martin, M. Gräf, T. Kramer, C. Jooss, M.-J. Choe, K. Thornton and K.-M. Weitzel, *Phys Chem Chem Phys*, 2017, **19**(15), 9762.
9. M. Schäfer and K.-M. Weitzel, *Materials Today Physics*, 2018, **5**, 12.
10. V.H. Gunawan, M. Schäfer and K.-M. Weitzel, *Phys Chem Chem Phys*, 2024, **26**(19), 14430.
11. C.J. SIMMONS, *Journal of the American Ceramic Society*, 1981, **64**(4), 200.
12. V.M. Sglavo and D.J. Green, *Journal of the American Ceramic Society*, 2001, **84**(8), 1832.
13. T.-S. Sheu and D.J. Green, *J Mater Sci*, 2007, **42**(6), 2064.
14. S. Berneschi, G.C. Righini and S. Pelli, *Applied Sciences*, 2021, **11**(10), 4610.
15. J. Saarinen, S. Honkanen, S.I. Najafi and J. Huttunen, *Appl Opt*, 1994, **33**(16), 3353.
16. P.L. Auger and S.I. Najafi, *Appl Opt*, 1994, **33**(16), 3333.
17. D. Budina, J. Zakel, J. Martin, P. Menezes, M. Schäfer and K.-M. Weitzel, *Zeitschrift für Physikalische Chemie*, 2014, **228**(4-5), 609.
18. M. Schäfer, D. Budina and K.-M. Weitzel, *Phys Chem Chem Phys*, 2019, **21**(47), 26251.

19. P.V. Menezes, J. Martin, M. Schäfer, H. Staesche, B. Roling and K.-M. Weitzel, *Phys Chem Chem Phys*, 2011, **13**(45), 20123.
20. M. Schäfer and K.-M. Weitzel, *Phys Chem Chem Phys*, 2011, **13**(45), 20112.
21. L. Rossrucker, P.V. Menezes, J. Zakel, M. Schäfer, B. Roling and K.-M. Weitzel, *Zeitschrift für Physikalische Chemie*, 2012, **226**(5-6), 341.
22. J. Zakel, P.V. Menezes, M. Schäfer and K.-M. Weitzel, *Solid State Ionics*, 2013, **242**, 20.
23. K. Rein and K.-M. Weitzel, *J. Mater. Chem. A*, 2024, **12**(23), 14117.
24. J.L. Wiemer, M. Schäfer and K.-M. Weitzel, *J. Phys. Chem. C*, 2021, **125**(9), 4977.
25. I. Svare, F. Borsa, D. Torgeson and S. Martin, *Journal of Non-Crystalline Solids*, 1994, **172-174**, 1300.
26. A. Hein, J. Martin, M. Schäfer and K.-M. Weitzel, *J. Phys. Chem. C*, 2017, **121**(6), 3203.
27. L. Onsager, *Phys. Rev.*, 1931, **37**(4), 405.
28. Heitjans P, editor, *Diffusion in Condensed Matter*: *Methods, Materials, Models,* Springer-Verlag Berlin Heidelberg, Berlin, Heidelberg, 2005.
29. C. Chatzichristodoulou, W.-S. Park, H.-S. Kim, P.V. Hendriksen and H.-I. Yoo, *Phys Chem Chem Phys*, 2010, **12**(33), 9637.
30. M. Landstorfer and T. Jacob, *Chem Soc Rev*, 2013, **42**(8), 3234.
31. K.D. Fong, H.K. Bergstrom, B.D. McCloskey and K.K. Mandadapu, *AIChE Journal*, 2020, **66**(12).
32. E. Whittaker and R. Muntus, *Geochimica et Cosmochimica Acta*, 1970, **34**(9), 945.
33. B. Bhushan and V.N. Koinkar, *Applied Physics Letters*, 1994, **64**(13), 1653.
34. M.D. Taylor, K.S. Choi, X. Sun, D.K. Matlock, C.E. Packard, L. Xu and F. Barlat, *Materials Science and Engineering: A*, 2014, **597**, 431.
35. K. Durst, O. Franke, A. Böhner and M. Göken, *Acta Materialia*, 2007, **55**(20), 6825.
36. R. Gy, *Materials Science and Engineering: B*, 2008, **149**(2), 159.
37. K.-M. Weitzel, *Meet. Abstr.*, 2024, **MA2024-02**(69), 4827.

The data presented in this work will be made available through a repository (https://doi.org/10.17192/openumr/524).